Excited-state absorption in Pr^{3+}:$Y_3Al_5O_{12}$

Y. M. Cheung and S. K. Gayen

Department of Physics and Engineering Physics, Stevens Institute of Technology, Hoboken, New Jersey 07030

(Received 27 December 1993)

The optical-absorption transitions originating from the lowest $4f5d$ excited state of Pr^{3+} in $Y_3Al_5O_{12}$ have been studied. The experimental arrangement uses a 7-ns 266-nm light pulse to populate the lowest $4f5d$ state, and a spatially overlapped, time-sequenced pulse from a frequency-tunable dye laser to induce transitions from that excited state. The excited-state-absorption (ESA) spectrum covering the 900–300-nm probe wavelength range is characterized by two broad peaks centered at 700 and 350 nm on a slowly rising background. The peak ESA cross section at 355 nm is $(1\pm0.1)\times10^{-17}$ cm^2. The position, shape, and strength of the spectrum suggest that the terminal states of the ESA transitions are the second $4f5d$ state of Pr^{3+} and the conduction band of the host lattice. The ESA measurements have been extended to transitions from the $^3P_0$ and $^1D_2$ excited states of the $4f^2$ configuration of Pr^{3+} as well. The ESA cross sections at a probe wavelength of 532 nm are $(8\pm1)\times10^{-19}$ cm^2 and $(5.7\pm0.6)\times10^{-19}$ cm^2 for transitions from the $^3P_0$ and $^1D_2$ excited states, respectively. The terminal state of ESA transitions from these two levels is the lowest $4f5d$ state. The strong ESA completely inhibits the potential laser action based on emission from these states in this crystal.

I. INTRODUCTION

Excited-state absorption (ESA) is a major loss mechanism that impedes, and in extreme cases, completely inhibits laser action in many optically active media. ESA involves absorptive transitions from a populated excited state of a material to even higher-energy excited states. The detrimental effect of ESA on potential laser action of a material is most pronounced when the ESA spectrum originating from an excited state happens to overlap with the fluorescence spectrum from the same initial state. Such an overlap is common in many tunable solid-state laser materials because of their broadband absorption and emission characteristics. If ESA cross section is smaller than the emission cross section, the effect is a reduction of the gain and effective tuning range. For an ESA cross section larger than the gain cross section, any possible laser action is completely quenched. Such a complete inhibition of potential laser operation is observed in Pr^{3+}:$Y_3Al_5O_{12}$ (YAG), and constitutes the subject matter of this article.

Excited-state absorption processes have been studied in detail in several high- and intermediate-field transition-metal ion-based crystals.[1-10] Both sharp and broad transitions from the metastable ^2E and $^2T_1$ states of Cr^{3+} were observed in ruby, emerald, and Cr^{3+}:MgO crystals.[1] The deleterious role of ESA, both in the lasing[2]- and the pump[3]-wavelength regions, on the laser performance of alexandrite (Cr^{3+}:BeAl$_2$O$_4$) was explored by Shand, Wal-

ling, and Morris. Similar studies have subsequently been extended to other vibronic laser crystals such as Cr^{3+}-doped K$_2$NaScF$_6$,[4] Gd$_3$Sc$_2$Ga$_3$O$_{12}$(GSGG),[4,5] Gd$_3$Sc$_2$Al$_3$O$_{12}$(GSAG),[4] Na$_3$Ga$_2$Li$_3$F$_{12}$,[6] LiCaAlF$_6$,[7] V^{2+}-doped KMgF$_3$ and MgF$_2$,[8,9] and Ni^{2+}-doped MgF$_2$ and MgO.[10] The ESA transitions in the lasing-wavelength regions of these crystals terminate on states belonging to the same configuration of the lasing ion, and have typical cross sections in the 10^{-21}–10^{-20} cm^2 range,[2-10] while ultraviolet transitions to charge-transfer states in Cr^{3+}:GSGG are characterized by a much higher cross section[4] on the order of 10^{-17} cm^2. ESA appears to be more severe a problem for lasers based on $5d\rightarrow4f$ transitions in trivalent rare-earth (R^{3+}) ion-doped crystals. In Ce^{3+}:YLiF$_4$, an ESA from the lasing level to the host conduction band leads to formation of color centers which degrade the gain and slope efficiency, limit the repetition rate for pulsed operation, and increase the lasing threshold.[11] Strong ESA transitions to the second $5d$ state and the host conduction band completely eliminates the lasing potential of Ce^{3+} in $Y_3Al_5O_{12}$.[12-14] The ESA cross section for these transitions are on the order of 10^{-18}–10^{-17} cm^2. More recently, strong ESA at a probe wavelength of 224 nm has been reported in four Pr^{3+}-doped fluoride crystals: CaF$_2$, SrF$_2$, LiYF$_4$, and BaY$_2$F$_8$.[15] In Pr^{3+}LiYF$_4$, these authors measured an ESA cross section of $2.6\pm0.5\times10^{-18}$ cm^2 at 224 nm which corresponds to a local emission peak characterized by an emission cross section of $2.0\pm0.2\times10^{-18}$ cm^2.

Y. M. CHEUNG AND S. K. GAYEN

The ESA transition initiates from a $4f5d$ state of Pr^{3+} and terminates on the conduction band of the host crystal.

In this article, we present a study of the optical transitions both from the lowest $4f5d$ state as well as the $^3P_0$ and $^1D_2$ states of the $4f^2$ configuration of Pr^{3+} in $Y_3Al_5O_{12}$. Narrowband laser action based on fluorescence originating from the $^3P_0$ and $^1D_2$ states of Pr^{3+} in several crystalline hosts have been reported.[16] Laser action based on those transitions may be expected in Pr^{3+}:YAG as well. More importantly, a number of characteristics indicated the potential of this crystal as an active material for a tunable solid-state laser operating in the near-ultraviolet-to-blue spectral region. First, the crystal fluoresces with near-unity quantum efficiency[17] over the 310–450 nm spectral range as displayed in Fig. 1. The fluorescence transitions originate from the lowest $4f5d$ state and terminate on ^3H_J ($J = 4,5,6$) multiplets of the $4f^2$ configuration. The centroids of the $^3H_5$ and $^3H_6$ multiplets are approximately 2500 and 5300 cm^{-1} above the ground level. Even the higher-lying levels of the $^3H_4$ multiplet lie at or above 533 cm^{-1} from the lowest level.[18] Because of the large energy gaps, thermal equilibrium population in these levels are negligibly small. So, they may serve as the ideal terminal states for four-level mode of laser operation. Second, the emission cross section for these parity-allowed electric-dipole transitions is on the order of $\sim 10^{-18}$ cm^2, two orders of magnitude higher than those for Cr^{3+}-doped tunable laser crystals. Third, since the energy gap between the lowest $4f5d$ state and the highest level of the $4f^2$ configuration is $\sim 10\,000$ cm^{-1}, the nonradiative decay is negligible.[17] The fluorescence lifetime remains fairly constant from 60–300 K. Fourth, the strong absorption bands covering the 300–180 nm spectral range make the crystal ideal for optical pumping. Fifth, YAG crystal is hard, has high thermal conductivity, and is an ideal host for both rare-earth and transition-metal ions. Finally, large crystals of high optical quality may be readily grown using the Czochralski technique. H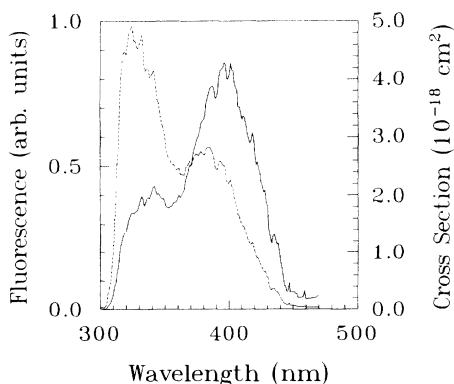owever, neither the inter- nor the intraconfigurational transitions mentioned above may lead to build up of laser oscillation in this crystal. On the contrary, the crystal shows net optical loss in all the channels mentioned above, indicative of very strong excited-state absorption.

The remainder of this article is organized as follows. In Sec. II, we briefly outline the excite-and-probe experimental arrangement used for measuring the ESA losses. Section III presents the formalism used for extracting ESA cross section from the measured probe transmittance. Section IV displays the experimental results. The implications of these measurements are discussed in Sec. V, and conclusions are summarized in Sec. VI.

II. EXPERIMENTAL ARRANGEMENT

The ESA spectrum was measured using the standard excite-and-probe technique. In this technique, the transmission of a weak probe pulse in the presence of a spatially overlapped, time-sequenced, strong pump pulse is compared to that in the absence of the pump pulse to determine the ESA coefficient and cross section at the particular probe wavelength being used. The strong pump pulse resonantly excites a transition in the sample creating a significant population in the excited state. The time-delayed probe pulse initiates transitions from the populated excited state to another higher-energy state. By continuously tuning the wavelength of the probe pulse, the spectrum of transitions originating from the excited state is obtained.

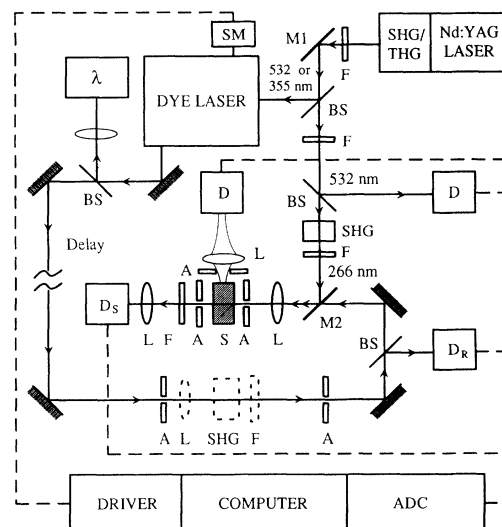The experimental arrangement for ESA measurements is shown schematically in Fig. 2. The 266-nm, 7-ns,

FIG. 1. The room-temperature emission spectra of 0.4% Pr^{3+}:YAG for 266-nm excitation of the lowest $4f5d$ state. The dashed curve represents the fluorescence intensity corrected for the equipment response. The solid line shows the emission cross section corrected for wavelength-dependence of line-shape function as described later in the text.

FIG. 2. A schematic diagram of the experimental arrangement used for ESA measurement. Key: A = aperture, ADC = analog-to-digital converter, BS = beam splitter, D = photo detector, F = filter, L = lens, λ = monochromator, M1, M2 = dielectric mirrors, SHG, THG = second and third harmonic generators, respectively, S = sample, SM = stepper motor. The lens-SHG-filter combination shown by dashed lines is inserted when the second harmonic of the dye laser is used as the probe beam.

fourth-harmonic pulses from a 10-Hz repetition-rate Q-switched Nd:YAG laser (Spectra Physics DCR-3G) were used as pump pulses to excite the lowest $4f5d$ state. The ground-state absorption (GSA) coefficient for excitation of the higher-energy end of the absorption band at this wavelength is 5.1 cm^{-1}. The pump beam was focused to a 180-μm nominal e^{-1}-radius spot on the sample using a 15-cm uv-quartz lens. The energy per pump pulse was maintained at 0.2 mJ. The pump-beam energy was monitored by measuring a fraction of the sample fluorescence at right angles to the direction of the pump beam. The pump-pulse energy was maintained well below the level for saturation of absorptive transition. The probe pulses were generated by a dye laser pumped by the 532- and 355-nm pulses from the same Nd:YAG laser. Solution of several organic dyes in methanol were used to cover the near-infrared to blue spectral region. Exciton dyes LDS 867, 821, 765, 750, 698, DCM, Rhodamine 640, 610, 590, and Fluorescein 548 pumped by the 532-nm pulses provided continuously tunable probe pulses from 900–540 nm. Probe pulses in the 545–410-nm range were obtained by pumping the Coumarin 500, 480, 440, and Stilbene 420 dye solutions by 355-nm pulses. For still shorter probe wavelengths, the near-infrared and red radiations from the dye laser were frequency doubled using a KD*P crystal, shown by dashed lines in Fig. 2. The dye laser was tuned by angle tuning the blazed grating which acts as the back mirror of the dye-laser cavity by a computer-controlled stepping motor. Details of the dye-laser construction and output characteristics have been presented in an earlier publication[19] and will not be repeated here. The probe beam was optically delayed with respect to and was then made collinear with the pump beam and focused onto the sample by the same quartz lens. The overall delay between the pump and the probe pulses was kept fixed at 12 ns. Since both the pump and the probe pulses were derived from the same initial pulse, the rms jitter in the time interval between them was much smaller than the width of either pulse. Nominal probe-pulse e^{-1} radius was 70 μm. The peak probe-pulse energy was maintained at $\sim$100 nJ using adequate neutral-density filters in order not to perturb the excited-state population. A small fraction of the dye-laser beam energy was sent to a monochromator for wavelength calibration.

The probe-pulse energy before the sample was monitored by directing a fraction of the pulse energy to a photodetector (D_R) by a beam splitter. The transmitted probe-pulse energy was measured by an identical detector (D_S) placed 1 m behind the sample. In the near-infrared and visible spectral regions photodiodes calibrated against a laser energy meter were used as detectors, while in the uv region photomultiplier tubes with S-20 response were used. Depending on the wavelength of the probe beam, cutoff filters were placed between the sample and the detector to block the pump beam and the pump-induced Pr^{3+} fluorescence from reaching the detector. In addition to the cutoff filters, a narrow aperture placed just after the sample and the large separation between the sample and the detector also helped minimize the background due to sample fluorescence. Furthermore, active

background subtraction, as outlined in the following section, was used to account for any residual fluorescence, scattered laser light and electronic noise.

The outputs of the photodetectors were sensed by identical gated integrators and read by 12-bit analog-to-digital converters interfaced to an IBM AT compatible microcomputer. Short-term random fluctuations and wavelength-dependent variations in the probe-beam intensity were corrected for by taking the ratio of the transmitted probe signal (measured by D_S) to the output of the reference detector (D_R). This normalized probe intensity was averaged over 100 laser shots to ensure an adequate signal-to-noise ratio. Data collection for a particular probe wavelength and for a fixed delay between the pump and the probe pulses involved measurement of the normalized probe intensity in the following sequence: (a) with the pump beam blocked and the probe beam incident on the sample (I_u), (b) with both the pump and probe beams incident on the sample (I_p), (c) with only the pump beam incident on the sample and the probe blocked (I_f), and (d) with both the beams blocked (I_n). I_n is a measure of background due to the electronic noise and the scattered light entering the detector, while I_f includes the pump-induced fluorescence background as well. As mentioned earlier, each of these four intensities were averaged over 100 laser shots for improving the signal-to-noise ratio. The ESA cross section for that particular wavelength was extracted from this data using the analysis method to be presented in the following section. The stepper motor then tuned the dye laser to a new wavelength and the whole sequence was repeated again.

The single-crystal Pr^{3+}:YAG sample used in all the measurements reported here was grown by the Czochralski method at the Crystal Products Division of Union Carbide. It contains 0.4% of the Pr^{3+} ion, which is equivalent to a concentration of 5.5×10^{19} $ions/cm^3$. The crystal is a 6-mm-long cylinder with its axis collinear with the [111] crystallographic axis. The exciting radiation for all measurements was incident along this axis of the sample.

III. ANALYSIS METHOD

The ESA coefficient α^* depends on the concentration of active ions in the excited state. The excited-state ion concentration, in turn, is determined by the energy density absorbed by the sample from the pump beam. In this section we closely follow Ref. 12 with some modifications to derive a relationship between the ESA cross section and the pump- and probe-beam parameters. The cross section may then be determined from the experimentally measured transmitted probe intensities.

The pump beam may be described by a photon flux $F(x,y,z,t)$ in photons/cm^2 s moving down the z axis. For a confocal parameter larger than the sample length L, the flux may be written as $F(x,y,z,t)=N(z)J(x,y)S(t)$, where $N(z)$ is the number of photons in the beam, and $J(x,y)$ and $S(t)$, are unity-normalized transverse-spatial and temporal profiles of the beam, respectively. The instantaneous excited-state ion concentration $c^*(x,y,z,t)$ may be expressed by the population rate equation

$$\frac{dc^*}{dt} = \alpha\beta F - \frac{c^*}{\tau} , \tag{1}$$

where α is the ground-state absorption (GSA) coefficient at the pump wavelength and β is the pumping quantum efficiency. Assuming that the pump pulse does not saturate the absorption transition so that Beer's law, $dF = -\alpha F dz$, accurately describes the change in the pump flux in an infinitesimal sample length dz, the excited-state ion concentration may be written as

$$c^*(x,y,z,t) = \alpha\beta N(0)J(x,y)e^{-\alpha z}e^{-t/\tau}$$
$$\times \int_{-\infty}^{t} S(t')e^{t'/\tau}dt' , \tag{2}$$

where $N(0)$ is the number of pump photons incident on the front surface of the sample at $z = 0$.

The probe beam may similarly be described by a flux $f(x,y,z,t) = n(z)j(x,y)s(t)$. The ions in the excited state absorb this probe beam. In addition, depending on the energy-level structure of the system there may be GSA of the probe beam. If the probe-beam wavelength is within the gain bandwidth of the sample, its intensity may be amplified. So, the overall change in the probe flux as it traverses a length element dz of the sample is

$$df = \{ -\sigma^* c^*(x,y,z,t_d) - \sigma_g c_g(x,y,z,t_d)$$
$$+ \sigma_e c^*(x,y,z,t_d)\} f(x,y,z,t_d)dz , \tag{3}$$

where, t_d is the pump-to-probe delay time, σ^*, σ_g, and σ_e are cross sections per ion for ESA, GSA, and emission, respectively, and c_g is the instantaneous ground-state ion concentration. Substituting from Eq. (2) in Eq. (3), and integrating over the transverse spatial coordinates x and y, we obtain

$$dn_p(z) = [-\sigma_g c_0 - (\sigma^* - \sigma_g - \sigma_e)\alpha\beta N(0)WTe^{-\alpha z}]$$
$$\times n(z)dz , \tag{4}$$

where the subscript p stands for pumped condition of the sample, $c_0 = c^* + c_g$, is the total ion concentration in the sample,

$$W = \int_{-\infty}^{\infty} \int_{-\infty}^{\infty} j(x,y)J(x,y)dx\,dy , \tag{5}$$

and

$$T = \int_{-\infty}^{\infty} \int_{-\infty}^{t} s(t-t_d)S(t')\exp[-(t-t')/\tau]dt'dt , \tag{6}$$

are the overlap integrals between the pump and probe spatial and temporal profiles, respectively. Equation (4) may now be integrated over the length of the sample L to yield

$$\ln\left[\frac{n(0)}{n_p(L)}\right] = \sigma_g c_0 L + (\sigma^* - \sigma_g - \sigma_e)\beta N(0)$$
$$\times LW(1-e^{-\alpha L})T , \tag{7}$$

where $n(0)$ and $n_p(L)$ are the number of incident and transmitted probe photons when the sample is excited by the pump beam. In the absence of the pump beam, the

probe may only be absorbed by the ions in the ground state, and the relation equivalent to Eq. (7) for the unpumped case is

$$\ln\left[\frac{n(0)}{n_u(L)}\right] = \sigma_g c_0 L . \tag{8}$$

The change in absorbance of the probe beam induced by the pump beam $A(t_d)$ is obtained by subtracting Eq. (8) from Eq. (7)

$$A(t_d) \equiv \ln\left[\frac{n_u(L)}{n_p(L)}\right] = (\sigma^* - \sigma_g - \sigma_e)\beta N(0)$$
$$\times LW(1-e^{-\alpha L})T , \tag{9}$$

where $n_u(L)$ is the number of probe photons when the sample is not pumped. This change in absorbance at a particular probe wavelength and for a pump-to-probe delay t_d can be readily obtained from the experimentally measured transmitted-probe intensities described in the previous section

$$A(t_d) = \ln\left[\frac{I_u - I_n}{I_p - I_f}\right] , \tag{10}$$

where I_p, I_u, I_f, and I_n are transmitted-probe intensity when the sample is illuminated by both the pump and the probe, only the probe, only the pump and neither, respectively.

The expression in Eq. (9) describes the change in probe absorption in the fluorescence region of the sample when both the ground- and excited-state absorption transitions are possible. Outside the gain region $\sigma_e = 0$, and if there is no ground-state absorption, $\sigma_g = 0$. If σ_e is sufficiently larger than σ^* for the single-pass gain to overcome the ESA and other cavity losses, laser action may still be possible, as in alexandrite.[2] But for $\sigma_e < \sigma^*$, the probe will experience net loss, as in Ce^{3+}:YAG.[12−14]

The beam overlap integrals W and T defined in Eqs. (5) and (6) may be evaluated analytically for beams characterized by well-defined spatial and temporal profile functions. Alternately, the profiles may be measured and the integrals may be evaluated numerically. The details of the numerical integration procedure for evaluating the spatial overlap have been presented in the appendix of Ref. 12.

IV. EXPERIMENTAL RESULTS

A. ESA transitions from the lowest $4f5d$ state

1. ESA dynamics and cross section

The 266-nm pump pulse excites the higher-lying vibrational levels of the lowest $4f5d$ state. Subsequent vibrational relaxation of these levels populates the zero vibrational level and lower-lying vibrational levels of that state. The vibrational relaxation within the same state of a d electron is known to be extremely rapid, with typical relaxation time in the ps range.[20,21] The upper limit for nonradiative relaxation time from the second to the first

$4f5d$ state in Pr^{3+}:$Y_3Al_5O_{12}$ has been estimated to be 500 ps.[17] The intra- $4f5d$(1) state relaxation time is expected to be much shorter. So, the excitation of the zero-vibrational level and lower-lying vibrational levels of the $4f5d$(1) state following 266-nm pumping may be considered to be almost instantaneous when compared with the fluorescence lifetime, as well as the time delay between and widths of the pump and the probe pulses. For several nanoseconds time delay between the pump and the probe pulses, the ESA transitions may be considered to originate from the populated zero vibrational level and the lower-lying vibrational levels of the $4f5d$(1) state. In order to verify this, we have measured the ESA coefficient as a function of the pump-to-probe time delay, and the results are presented in Fig. 3. The solid line is a theoretical fit to the experimental data represented by open circles assuming a 26-ns excited-state lifetime, and Gaussian temporal profiles for the pump and the probe pulses. The excellent agreement affirms that the lowest $4f5d$ state is the dominant initial state for ESA transitions. In principle, ESA transitions from the populated $^3P_0$ and $^1D_2$ states are possible and may contribute to the observed signal. However, the branching ratios for transitions which may populate these two states following the excitation of $4f5d$ states are approximately two orders of magnitude smaller than fluorescence transitions to the ^3H_J ($J=4,5,6$) states. So, those states are not significantly populated, especially in the nanosecond time scale used in this measurement.

This time-dependent measurement also indicates that the ESA reaches the peak value at a pump-to-probe time delay of ~10 ns. We maintained a time delay of ~12 ns for all the subsequent measurements to obtain adequate ESA signal. Intense excitation by the pump pulse may, in principle, lead to nonlinear processes such as saturation of GSA and multiphoton absorption. In order to examine if those processes were operative at the intensity level used in this experiment, we measured the ESA coefficient as a function of the energy of the pump pulse. The simple linear relationship, as presented in Fig. 4, seems to rule out any significant interference from nonlinear processes.
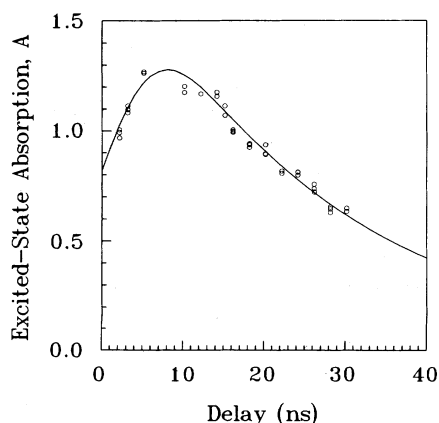

FIG. 3. Evolution of excited-state absorption as a function of time delay between the 266-nm pump pulse and the 355-nm probe pulse measured at room temperature.
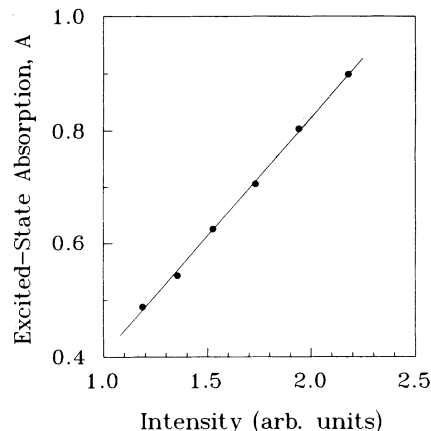

FIG. 4. Dependence of excited-state absorption on the energy of the 266-nm pump pulse. The 532-nm probe pulse was delayed by 12 ns with respect to the pump pulse. A linear variation indicates absence of any higher-order process. The pump intensity was maintained at approximately the middle of the range indicated in the figure for all subsequent measurements.

The ESA cross section σ^* can be calculated from measured $A(t_d)$ using Eq. (9). The transverse spatial profiles of the pump and the probe pulses were measured by scanning a razor blade across the beams at the sample position in both the vertical and the horizontal directions. The spatial overlap integral W was then evaluated numerically following the procedure detailed in the appendix of Ref. 12. Assuming a pumping efficiency β of unity, the ESA cross section is determined to be $(1\pm0.1)\times10^{-17}$ cm^2 at a probe wavelength of 355 nm, and $(5.5\pm0.5)\times10^{-18}$ cm^2 at 532 nm.

2. ESA spectrum

The probe-wavelength dependence of ESA originating from the lowest $4f5d$ state of Pr^{3+}:YAG is shown in Fig. 5. Fourteen different dyes as well as the second harmonic of some of the dyes, as detailed in Sec. II, were used to construct this composite spectrum. For spectrally adjacent dyes, measurements were made at overlapping wavelengths to determine the near-unity scale factors needed to account for the small alignment and overlap variations due to dye changes.

Experimentally, one measures the difference in cross section $(\sigma^*-\sigma_g-\sigma_e)$ as a function of probe wavelength. The ESA cross section σ^* is determined from the difference spectrum and the values of σ_g and σ_e obtained from independent measurements. Except for the weak and sharp absorption and emission transitions involving the ^3P_J and $^1I_6$ manifolds around 480 nm and the $^1D_2$ manifold around 608 nm, there is no GSA or emission in the 900–460-nm range. The GSA and emission cross section for transitions involving those states are on the order of 10^{-20}–10^{-19} cm^2. So, the difference and the ESA spectra may be considered to be identical in the 900–460-nm range. However, that is not the case for the shorter wavelength range. The strong fluorescence from the lowest $4f5d$ state spans the 450 to 310-nm range.
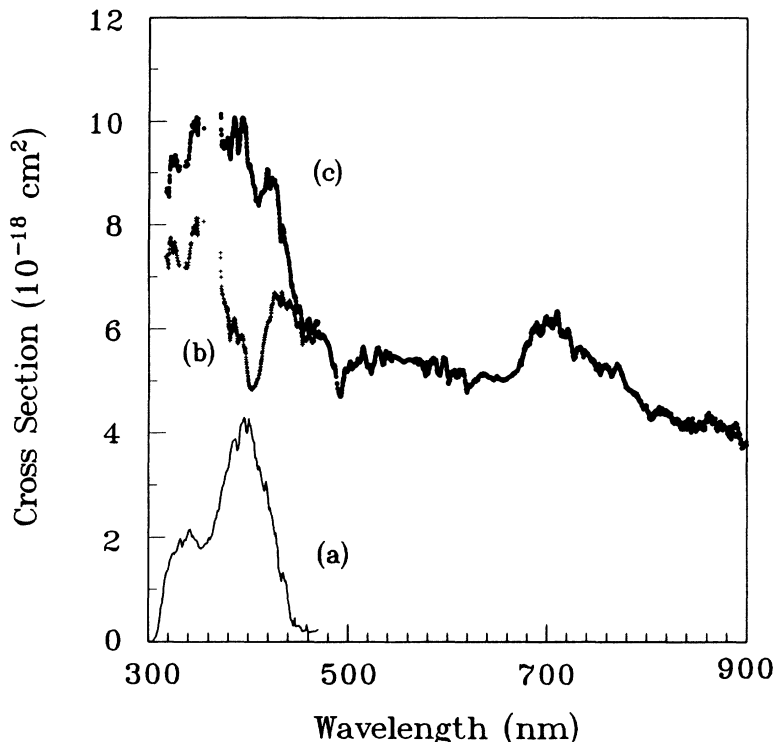
Y. M. CHEUNG AND S. K. GAYEN

FIG. 5. The dependence of (a) emission cross section σ_e, (b) difference in cross section $(\sigma^* - \sigma_g - \sigma_e)$, and (c) ESA cross section σ^* on wavelength. The ESA transitions originate from the lowest $4f5d$ state excited by the 266-nm radiation from a Nd:YAG laser. The gap in data points between 375–350 nm is due to a lack of proper arrangement to separate out the dye laser fundamental from its second harmonic.

The ESA cross section in this range has to be determined by adding the emission cross section to the difference. The emission cross section is determined from[22]

$$\sigma_e(v) = \frac{\lambda^2}{8\pi c n^2 \tau} g(v) \, , \tag{11}$$

where n is the index of refraction at wavelength $\lambda = v^{-1}$. The normalized line-shape function $g(v)$ is obtained from the emission spectrum using the relation[23]

$$g(v) = \frac{\lambda^6 I(\lambda)}{\int \lambda^4 I(\lambda) d\lambda} \, , \tag{12}$$

where $I(\lambda)$ is the luminescence intensity per unit wavelength interval $(\mathrm{Wm}^{-2}\,\mathrm{nm}^{-1})$ at wavelength λ. The emission cross section as a function of wavelength thus determined is presented in Fig. 1 and in the curve (a) of Fig. 5. Curve (b) in Fig. 5 shows the difference spectrum, while curve (c) represents the ESA spectrum obtained by adding the emission cross section to the difference.

Except for the broad, shallow peak around 700 nm, the ESA cross section in the 900–450-nm range increases gradually from 4×10^{-18} cm^2 to 6×10^{-18} cm^2. At shorter wavelengths, there is a dip in the difference spectrum which corresponds to the peak of the emission cross section spectrum. The overall ESA cross section increases rapidly at wavelengths shorter than 450 nm with a peak around 355 nm and gradually decreases at even shorter wavelengths.

In order to obtain an estimate of the overall strength of the ESA transitions we calculated the oscillator strength by numerically integrating the cross section over the ESA spectrum. Using

$$f = (1.13 \times 10^{12}) \frac{9n}{(n^2+2)^2} \int \sigma^*(\lambda) \frac{d\lambda}{\lambda^2} \, , \tag{13}$$

where the index of refraction of YAG is taken to have the average value of 1.82, the oscillator strength f is estimated to be 0.1. Since, we do not have the complete ESA spectrum to calculate the value of oscillator strength, the total oscillator strength will be somewhat higher.

B. ESA from $^3P_0$ and $^1D_2$ states

We have also measured excited-state absorption originating from the $^3P_0$ and $^1D_2$ states of the $4f^2$ configuration. The thrust of these measurements was to explore if ESA happened to be a significant loss mechanism for possible laser transitions originating from these states. So, ESA cross section was measured at a single-probe wavelength for both the cases, and no attempt was made to obtain the complete spectra.

For ESA measurement from the $^3P_0$ state, 452-nm radiation from the dye laser was used to resonantly excite the $^3P_2$ state. Since the ^3P_J ($J = 0, 1, 2$) manifolds overlap, rapid nonradiative relaxation populated the $^3P_0$ state. The ESA cross section at a probe wavelength of 532 nm was measured to be $(8 \pm 1) \times 10^{-19}$ cm^2. The peak emission cross section for transitions from this state calculated from the fluorescence spectrum using Eq. (11) is 1.1×10^{-19} cm^2, much smaller than the ESA cross section. If the energy of the $^3P_0$ state (20 534 cm^{-1}) is added to that of the probe photon (18 797 cm^{-1}), the resulting transition energy of 39 331 cm^{-1} corresponds to an excitation into the higher-energy tail of the $4f5d(1)$ state. So, it is reasonable to assign the terminal state of the ESA transition to be the $4f5d(1)$ state. The measured ESA cross section is typical for $4f^n \rightarrow 4f^{n-1}5d$ transitions in R^{3+} ion-doped crystals, and lends additional support to above assignment.

Support for this assignment is also obtained from similar ESA transitions in Sm^{2+}-doped SrF_2 and $SrCl_2$ reported previously.[24] The ESA transitions originate from the excited $^5D_0(4f^6)$ state and terminate on the states of the $4f^55d$ configuration of the Sm^{2+} ion. The ESA cross section at the operating energy of $14\,350$ cm^{-1} of the Sm^{2+}:SrF_2 laser was estimated to be 7×10^{-20} cm^2. As the authors point out, the $^5D_0 \rightarrow |^6F, e_g; S = 2\rangle$ transition that gives rise to the ESA band around $14\,350$ cm^{-1} is particularly weak, and the lasing transition fortuitously happens to be displaced from the peak of the band. So the gain may overcome the loss making the laser operation possible. In contrast, the $^3P_0 \rightarrow 4f5d$ ESA cross section in Pr^{3+}:YAG is approximately an order of magnitude larger and defeats the gain completely.

The fluorescence spectrum due to transitions from the $^3P_0$ state is highly structured even at room temperature. There are two major groups of fluorescence lines. The first group arising from $^3P_0 \rightarrow {}^3H_4$ transitions extends from 480–510 nm with the major peak at 488 nm. The second group due to $^3P_0 \rightarrow {}^3H_5$ transitions spans the 525–570-nm range. ESA transitions from the $^3P_0$ state at any probe wavelength in the 480–570-nm range will terminate on either the first or the second $4f5d$ state. The ESA cross sections for such interconfigurational transitions are expected to be comparable to that measured at the probe wavelength of 532 nm reported above.

In order to study the ESA process originating from the $^1D_2$ state, the dye laser was tuned to the peak of $^3H_4 \rightarrow {}^1D_2$ GSA transition at 609 nm. The ESA cross section at a probe wavelength of 532 nm was measured to be $(5.7 \pm 0.6) \times 10^{-19}$ cm^2. This should be compared to the peak emission cross section of 1.5×10^{-20} cm^2. Again the sum of the energy of the $^1D_2$ state ($16\,420$ cm^{-1}) and that of the probe photon leads to a transition energy of $35\,217$ cm^{-1} corresponding to an excitation into the $4f5d(1)$ state. The strength of visible fluorescence from the $^1D_2$ state is mainly concentrated in three sharp transitions to the 0, 19, and 50 cm^{-1} levels of the $^3H_4$ manifold. ESA transitions from the $^1D_2$ state at the probe wavelengths corresponding to these fluorescence lines will terminate on the low-energy end of the lowest $4f5d$ state, and are expected to be characterized by cross sections comparable to that measured at 532 nm. The emission wavelengths corresponding to transitions to the $^3H_5$ and even higher manifolds are sufficiently long so that no $^1D_2 \rightarrow 4f5d$ ESA transitions at these wavelengths are energetically possible. However, those emission transitions are in general very weak,[18] and efficient laser action based on these transitions is unlikely.

V. DISCUSSION

The ESA transitions both from the lowest $4f5d$ state as well as from the $^3P_0$ and $^1D_2$ states of the $4f^2$ configuration are of considerable practical and theoretical significance. On the practical side, the observed strong ESA seems to rule out the probable use of Pr^{3+}:YAG as a solid-state laser crystal in the visible and near-ultraviolet spectral region. On the other hand, the shape and the strength of the ESA spectrum originating

from the lowest $4f5d$ state raises interesting questions about the nature of the near-ultraviolet energy eigenstates of the crystal.

The single exponential decay of ESA with a characteristics decay time equal to that of the fluorescence lifetime for 266-nm pumping identifies the lowest-$4f5d$ state as the initial state for ESA transitions. However, the terminal state may not be so easily and uniquely identified. From one-photon absorption spectrum,[19] the second $4f5d$ band appears to be extending from 255 to 190 nm. If the measured energy of the zero-phonon transition[19] to the lowest-$4f5d$ state ($32\,552$ cm^{-1}) is added to the ESA transition energies, the 900–500-nm segment of the ESA spectrum will overlap with the second $4f5d$ absorption band. So, from energy consideration alone, it would be tempting to ascribe at least this part of the ESA spectrum to transitions to the second $4f5d$ state. The 700-nm ESA peak, corresponding to an overall transition energy of $46\,838$ cm^{-1} (213.5 nm), would then coincide with the middle of the broad, intense second $4f5d$ GSA band.

However, the situation is considerably more difficult. First, the stronger, higher-energy ESA band extends to approximately $64\,000$ cm^{-1}, and presumably even beyond. The measurement was limited by the available range of probe wavelength. This energy range is beyond the extent of the second $4f5d$ state, and may encompass even higher-energy states of the configuration. Second, the large ESA cross section on the order of 5×10^{-18} cm^2 even in the 900–500-nm region and the high oscillator strength ($f > 0.1$) are unlikely for transitions within the states of the same $4f5d$ configuration. This is even much stronger than the $^3P_0$, $^1D_2 \rightarrow 4f5d$ interconfigurational transition cross sections reported in the previous section.

Only two types of transitions in impurity-ion doped crystals are known to be characterized by such large oscillator strength: first, the photoionization transitions[12] to the conduction band (CB) of the host lattice; and second, the dopant$\leftrightarrow$ligand charge-transfer (CT) transitions.[25,26] Since, the characteristics of CT spectra of R^{3+} ions depend upon the properties of the hosts and not on the ions themselves,[27] and based on the nature of ESA transitions in Ce^{3+}:YAG, we consider an excited-state photoionization process to be a more probable mechanism for the observed strength of the ESA transitions in Pr^{3+}:YAG as well. Photoionization measurements from both the ground[28] and the excited states[12] may confirm this assignment. The excitation energy for the onset of photocurrent in these measurements would identify the location of the conduction-band edge. The position of the conduction-band edge is consistent with this assignment. The band gap of YAG (Ref. 29) is $50\,000$ cm^{-1}. An extrapolation on the longer-wavelength end of the ESA spectrum of Fig. 5 indicates that the CB edge lies approximately 8000 ± 500 cm^{-1} above the relaxed lowest $4f5d$ excited state. Since the position of the zero-vibrational level of the lowest $4f5d$ state with respect to the lowest level of the $^3H_4(4f^2)$ ground multiplet is known to be $32\,552$ cm^{-1}, the relative position of the Pr^{3+} energy levels within the YAG band gap may be determined, as illustrated in Fig. 6. The CB edge overlaps with the second $4f5d$ state, while the lowest level of
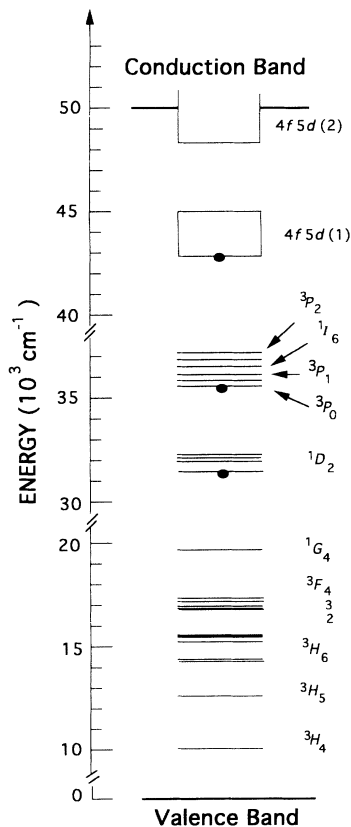
FIG. 6. A simplified energy-level diagram showing the positions of Pr^{3+} states relative to the valence and conduction bands of the YAG host. The states from which fluorescence has been observed are marked by solid ellipses.

the $4f^2$ configuration is approximately $10\,000$ cm^{-1} above the valence-band edge.

The wave functions describing the states at energies higher than the CB edge involve a superposition of delocalized Bloch states and the more localized d-like orbitals of the Pr^{3+} ion. This strong overlap between the higher-energy $4f5d$ states and the conduction band has important consequences for both the GSA transitions originating from the highly shielded lowest $4f^2$ state and the ESA transitions from the more-extended lowest $4f5d$ state. The GSA transitions are sensitive to both the states of the Pr^{3+} ion and the plane wave components of the conduction band. The strength of ESA transitions from the lowest $4f5d$ state, on the other hand, will be dominated by transition-matrix elements connecting the state to the delocalized Bloch states, and will be much less sensitive to the d-like states. In general, much higher density of final states is available for transition from localized impurity ion states to CB states as compared to that for intraion transitions, and this may contribute to the higher strength for the localized→delocalized transitions. The larger spatial extent of d orbitals compared to that for the f orbitals will tend to make the $5d$→CB transitions stronger than the $4f$→CB transitions. The exact mechanism that accounts for the large oscillator strength for the $5d$→CB ESA transitions is not well es-

tablished. However, a plausible model applicable for divalent rare-earth ions has recently been presented.[30] The model ascribes the large oscillator strength for the $4f^55d$→CB ESA transition in Sm^{2+}:CaF_2 to "intensity borrowing" from the valence→conduction-band transition. This intensity borrowing is proposed to be mediated by an estimated 50-50 admixture of the $Sm^{2+}5d$ orbital and the $2p$ orbitals on F^- of the CaF_2 host.

A quantitative calculation of the ESA transition strength and line shape in Pr^{3+}:YAG requires detailed knowledge of (a) the band structure of YAG crystal, (b) the appropriate CF-perturbed $4f5d$ wave functions, and (c) the effect of lattice relaxation that follows an electronic transition,[12] none of which is complete or readily available. So, a quantitative explanation of the measured ESA spectrum may not be possible at the moment. Some general observations may, however, be made about the shape and position of the spectra. The characteristics of transitions from a localized impurity-state in the band gap to the CB depend strongly on the characteristic volume of the initial-bound-state wave function.[31] In particular, the overlap integral involving the dopant wave function of characteristic radius a and the plane-wave state with wave vector k peaks[31] for $ka \sim 1$. Also the higher momentum-band states lie at higher energy. Since the wave function of a d electron is much more diffuse (larger a) than that of an f electron, $4f5d$→CB transition will have its maximum cross section at a significantly lower energy than that for $4f^2$→CB transition. Thus the shape and the peak position of ESA transitions are not related in any simple way to those of the GSA transitions.

VI. CONCLUSIONS

Strong excited-state absorption from the lowest $4f5d$ state as well as from the $^3P_0$ and $^1D_2$ states of the $4f^2$ configuration of Pr^{3+}:YAG has been observed. The ESA transitions originating from the lowest $4f5d$ state terminate on the mixed conduction band and dopant states. The peak cross section for these photoionization transitions is $(1.0\pm0.1)\times10^{-17}$ cm^2. The ESA transitions from the $^3P_0$ and $^1D_2$ states are interconfigurational, the final state is the lowest $4f5d$ state. Typical cross section for these transitions is approximately 5×10^{-19} cm^2. These ESA cross sections are much higher than the respective gain cross sections, and the ESA spectra overlap with the fluorescence spectra. The strong ESA thus completely inhibits the potential laser action in the visible and near-ultraviolet spectral regions in this crystal.

The location of the host conduction band relative to the fluorescing levels is an important design consideration for potential solid-state laser materials. Excited-state photoionization transitions in the fluorescence-wavelength region may impede or inhibit potential laser operation in otherwise promising crystals.

[1]W. M. Fairbank, Jr., G. K. Klauminzer, and A. L. Schawlow, Phys. Rev. B **11**, 60 (1975).

[2]M. L. Shand and J. C. Walling, IEEE J. Quantum Electron. **QE-18**, 1152 (1982).

[3]M. L. Shand, J. C. Walling, and R. C. Morris, J. Appl. Phys. **52**, 953 (1981).

[4]L. J. Andrews, S. M. Hitelman, M. Kokta, and D. Gabbe, J. Chem. Phys. **84**, 5229 (1986).

[5]W. Seelert and E. Strauss, Opt. Lett. **12**, 798 (1987).

[6]J. A. Caird, S. A. Payne, P. R. Staver, A. J. Ramponi, L. L. Chase, and W. F. Krupke, IEEE J. Quantum Electron. **24**, 1077 (1988).

[7]H. W. H. Lee, S. A. Payne, and L. L. Chase, Phys. Rev. B **39**, 8907 (1989).

[8]S. A. Payne, L. L. Chase, and G. D. Wilke, Phys. Rev. B **37**, 998 (1988).

[9]R. Moncorge and T. Benyattou, Phys. Rev. B **37**, 9177 (1989).

[10]R. Moncorge and T. Benyattou, Phys. Rev. B **37**, 9186 (1989).

[11]K. S. Lim and D. S. Hamilton, J. Opt. Soc. Am. **6**, 1401 (1989).

[12]D. S. Hamilton, S. K. Gayen, G. J. Pogatshnik, R. D. Ghen, and W. J. Miniscalco, Phys. Rev. B **39**, 8807 (1989).

[13]R. R. Jacobs, W. F. Krupke, and M. J. Weber, Appl. Phys. Lett. **33**, 410 (1978); W. J. Miniscalco, J. M. Pellegrino, and W. M. Yen, J. Appl. Phys. **49**, 6109 (1978).

[14]J. F. Owen, P. B. Dorain, and T. Kobaysi, J. Appl. Phys. **52**, 1216 (1983).

[15]J. K. Lawson and S. A. Payne, Opt. Mat. **2**, 225 (1993).

[16]For a listing of lasers based on Pr^{3+}-activated crystals, see A. A. Kaminskii, *Laser Crystals*, 2nd ed. (Springer-Verlag, Berlin, 1990), p. 381, and relevant references therein.

[17]M. J. Weber, Solid State Commun. **12**, 741 (1973).

[18]J. B. Gruber, M. E. Hills, R. M. McFarlane, C. A. Morrison, and G. A. Turner, Chem. Phys. **134**, 241 (1989).

[19]S. K. Gayen, B. Q. Xie, and Y. M. Cheung, Phys. Rev. B **45**, 20 (1992).

[20]S. K. Gayen, W. B. Wang, V. Petricevic, K. M. Yoo, and R. R. Alfano, Appl. Phys. Lett. **50**, 1494 (1987).

[21]S. K. Gayen, W. B. Wang, V. Petricevic, S. G. Demos, and R. R. Alfano, J. Lumin. **47**, 181 (1991), and relevant references therein.

[22]J. A. Caird, S. A. Payne, P. R. Staver, A. J. Ramponi, L. L. Chase, and W. F. Krupke, IEEE J. Quantum Electron. **24**, 1077 (1988).

[23]For the proper relationship between the line-shape function and the broadband emission spectrum see, A. J. Wojtowicz, M. Kazmierczak, A. Lempicki, and R. H. Bartram, J. Opt. Soc. Am. B **6**, 1106 (1989); and D. E. McCumber, Phys. Rev. **136**, A954 (1964).

[24]S. A. Payne, L. L. Chase, and W. F. Krupke, J. Chem. Phys. **88**, 6751 (1988).

[25]C. K. Jorgensen, in *Progress in Inorganic Chemistry*, edited by S. J. Lidiard (Wiley, New York, 1970), Vol. 12, p. 39.

[26]D. S. McClure, *Optical Properties of Ions in Solids*, edited by B. Di. Bartolo (Plenum, New York, 1975), p. 259.

[27]R. C. Ropp and B. Carroll, J. Phys. Chem. **81**, 1699 (1977).

[28]C. Pedrini, F. Rogemond, and D. S. McClure, J. Appl. Phys. **59**, 1196 (1986).

[29]G. A. Slack, D. W. Oliver, R. M. Chrenko, and S. Roberts, Phys. Rev. **177**, 1308 (1969).

[30]J. K. Lawson and S. A. Payne, J. Opt. Soc. Am. B **8**, 1404 (1991); and Phys. Rev. B **47**, 14003 (1993).

[31]B. K. Ridley, *Quantum Processes in Semiconductors*, 2nd ed. (Clarendon, Oxford, 1988), p. 204.